MATERIALS SCIENCE

# Large dipole moment induced efficient bismuth chromate photocatalysts for wide-spectrum driven water oxidation and complete mineralization of pollutants

Xianjie Chen[1], Yuan Xu[2], Xinguo Ma[2] and Yongfa Zhu[1,*]

## ABSTRACT

Herein, a wide-spectrum ($\sim$678 nm) responsive $Bi_8(CrO_4)O_{11}$ photocatalyst with a theoretical solar spectrum efficiency of 42.0% was successfully constructed. $Bi_8(CrO_4)O_{11}$ showed highly efficient and stable photocatalytic water oxidation activity with a notable apparent quantum efficiency of 2.87% (420 nm), superior to many reported wide-spectrum driven photocatalysts. Most remarkably, its strong oxidation ability also enables the simultaneous degradation and complete mineralization for phenol, and its excellent performance is about 23.0 and 2.9 times higher than CdS and P25-$TiO_2$, respectively. Its high activity is ascribed to the giant internal electric field induced by its large crystal dipole, which accelerates the rapid separation of photogenerated electron–hole pairs. Briefly, the discovery of wide-spectrum bismuth chromate and the mechanism of exponentially enhanced photocatalytic performance by increasing the crystal dipole throw light on improving solar energy conversion.

**Keywords:** bismuth chromate, dipole moment, internal electric field, water oxidation, complete mineralization

## INTRODUCTION

The conversion and utilization of solar energy for chemical fuel production and environmental remediation through artificial photocatalysis have been recognized to be an ideal route to address critical energy and environmental concerns [1–3]. The full utilization of solar light is a great challenge for achieving sufficient efficiency in practical applications. In the early stages, UV light-activated materials, such as $TiO_2$, $SrTiO_3$, $NaTaO_3$, etc., dominated photocatalysis study, due to the wide bandgap of conventional semiconductors and their strong redox capability of charge carriers for igniting chemical reactions [4–7]. Nonetheless, the extremely low ratio of UV photons in solar energy greatly hinders the ability to maximize the solar-to-chemical energy conversion efficiency. In recent years, a number of mixed-anion and non-oxide materials such as (oxy)nitrides and (oxy)sulfides have been developed as attractive broadband light-responsive photocatalysts [8–11]. The valence band maximums (VB) of the mixed-anion materials can be substantially regulated by hybridization of O 2p or other introduced anion orbitals, enabling both broadband light absorption and suitable band potentials for both reduction and oxidation of water [12,13]. For example, $BaNbO_2N$, reported by Hisatomi *et al.*, could broaden the light absorption up to 740 nm and simultaneously shows efficient water oxidation [14]. However, narrowing the bandgap of a photocatalyst weakens the driving force for redox reactions, especially water oxidation and pollutant degradation, because these reactions involve a complicated multi-electron process [15]. Therefore, the development of wide-spectrum responsive and highly efficient photocatalysts for water oxidation and pollutant degradation is a critical issue to be addressed at present.

Bi-based oxometallate materials, such as $BiVO_4$, $Bi_2WO_6$, $Bi_2MoO_6$, etc, have been widely studied as visible-light active photocatalysts, due to their high stability, abundant resources and low toxicity [16–19]. Moreover, they also exhibit excellent photocatalytic performance in water oxidation, which is mainly benefiting from their sufficiently deep VB

[1]Department of Chemistry, Tsinghua University, Beijing 100084, China and [2]School of Science, Hubei University of Technology, Wuhan 430068, China

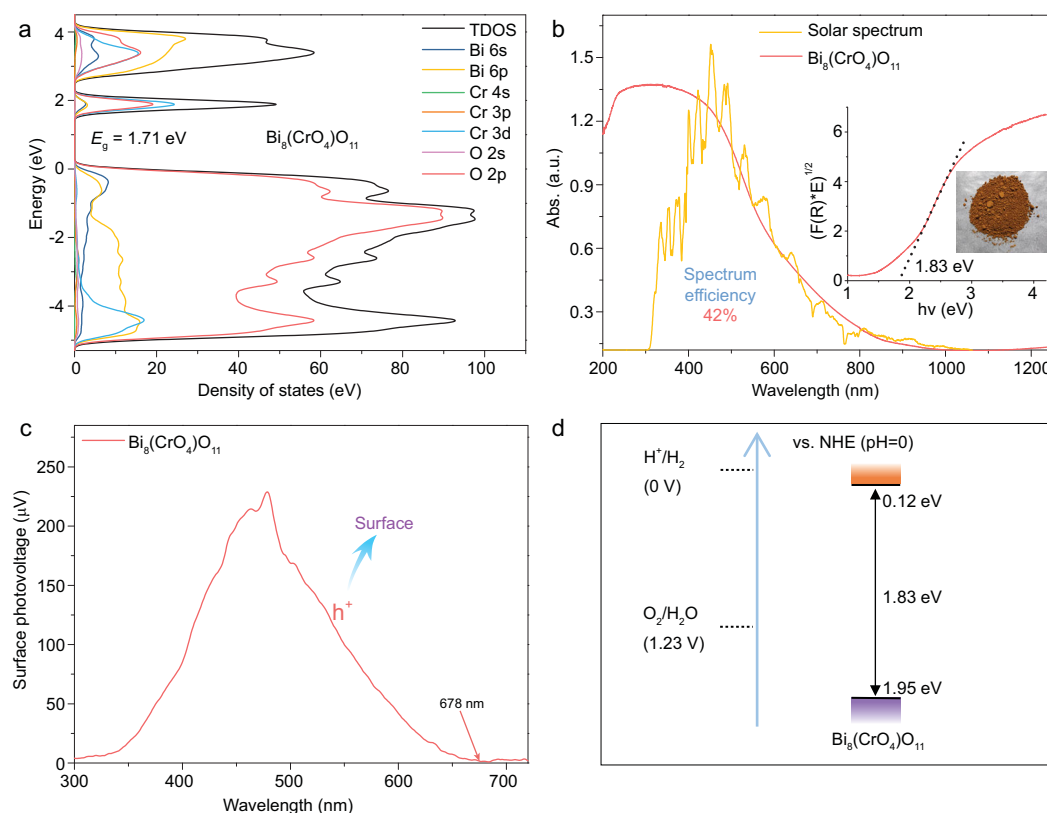*Corresponding author. E-mail: zhuyf@tsinghua.edu.cn

**Figure 1.** (a) The calculated density of state, (b) UV–vis–NIR DRS (the corresponding Tauc plots and a sample photograph appear in the inset), (c) the surface photovoltage spectrum, and (d) a schematic drawing of the redox potentials of $Bi_8(CrO_4)O_{11}$.

position as compared to the potential for water oxidation and pollutant degradation [20,21]. In particular, the $BiVO_4$ photocatalysts present highly efficient and stable water oxidation performance, and its highest solar-to-hydrogen energy conversion efficiency of 1.2% for Z-scheme pure-water splitting by coupling with $SrTiO_3$: La, Rh has been reported [22]. Nevertheless, their relatively wide bandgaps (about 2.5 eV) greatly limit their further application. Recently, research into Cr-based layered double hydroxide photocatalysts revealed that the hybridization of Cr 3d orbitals with O 2p orbitals in $[CrO_6]$ clusters shifts the conduction band minimum (CB) down and results in wide visible-light absorption [23,24]. Inspired by the above, the construction of bismuth chromate photocatalyst may be a desired route to achieve wide-spectrum driven, efficient, and stable photocatalytic performance.

In this work, a wide-spectrum responsive $Bi_8(CrO_4)O_{11}$ photocatalyst was successfully constructed. Owing to the hybridization of Cr 3d with O 2p orbitals shifting the conduction band minimum down, $Bi_8(CrO_4)O_{11}$ allows its absorption up to the entire visible region ($\sim$678 nm) with a theoretical solar spectrum efficiency of 42.0%. Moreover, attributed to the giant internal electric field (IEF) induced by its large dipole moment,

$Bi_8(CrO_4)O_{11}$ realized evidently rapid separation of photogenerated electron–hole pairs, thus showed highly efficient photocatalytic water oxidation activity with a notable apparent quantum yield of 2.87% (420 nm), superior to many reported wide-spectrum driven photocatalysts. Most remarkably, its strong oxidation ability also enables simultaneous degradation and complete mineralization for phenol, and its excellent performance is about 23.0 and 2.9 times higher than CdS and $P25$–$TiO_2$, respectively.

## RESULTS AND DISCUSSION

Herein, monoclinic $Bi_8(CrO_4)O_{11}$ nanorods (Figs S1–S3), a novel bismuth chromate photocatalyst, were successfully synthesized via a facile hydrothermal reaction. Then, density functional theory (DFT) was applied to calculate the electronic structure of this bismuth chromate. As shown in Fig. 1a, $Bi_8(CrO_4)O_{11}$ possesses a relatively small bandgap of 1.71 eV. Moreover, the density of state of $Bi_8(CrO_4)O_{11}$ reveals that its VB is mainly composed of O 2p and Bi 6s orbitals, in agreement with other Bi-based oxometallate photocatalysts, which could effectively avoid the self-oxidative deactivation by photogenerated holes. Also, its CB is mainly
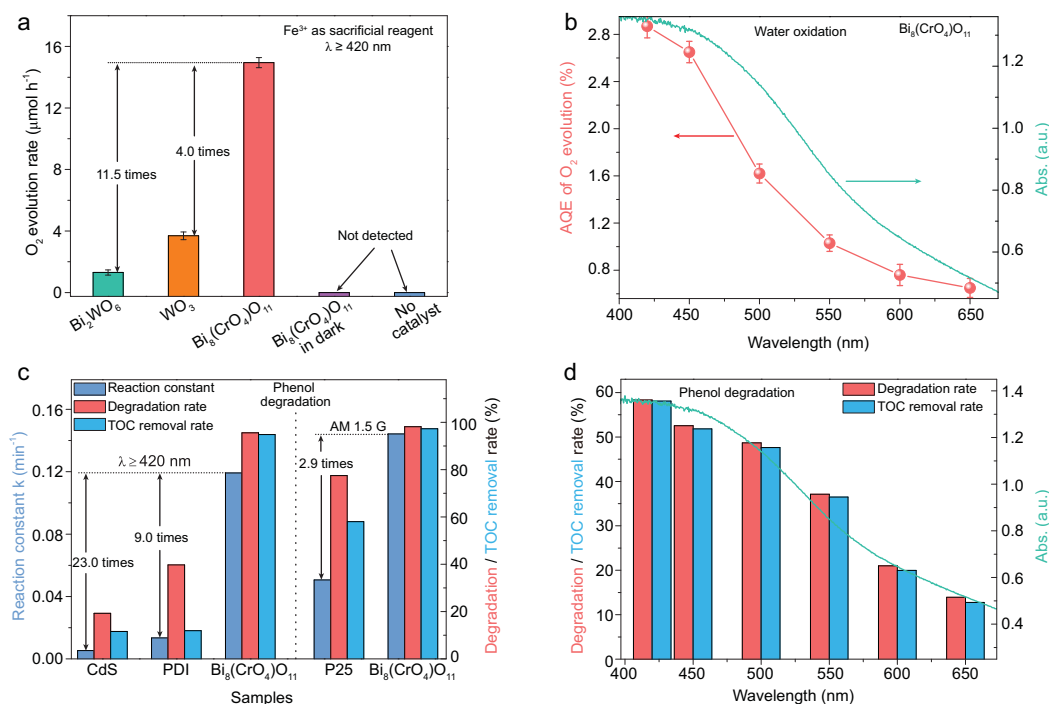
**Figure 2.** (a) A comparison of photocatalytic water oxidation activity over different photocatalysts. (b) The wavelength-dependent AQE of water oxidation over $Bi_8(CrO_4)O_{11}$. (c) A comparison of degradation rate constants, degradation rates and TOC removal rates of phenol over different photocatalysts. (d) The wavelength-dependent degradation rate and TOC removal rate of phenol over $Bi_8(CrO_4)O_{11}$.

provided by the hybridization of Cr 3d orbitals with O 2p orbitals, demonstrating that the introduction of the $[CrO_4]$ cluster plays a crucial role in extending absorption into the entire visible region. Moreover, the indirect band structure of $Bi_8(CrO_4)O_{11}$ is also confirmed by its electronic band diagram (Fig. S4a), which is in favor of confining the recombination of photogenerated electron–hole pairs. In the diffuse reflectance spectrum (DRS) (Fig. 1b), $Bi_8(CrO_4)O_{11}$ nanorod photocatalyst displays a quite broad absorption band, practically allowing light absorption up to the entire visible region, and its highest theoretical solar utilization could reach 42.0%. Almost consistent with the above DFT result, the bandgap of $Bi_8(CrO_4)O_{11}$ was calculated as 1.83 eV by the Kubelka–Munk function, which absolutely satisfies the thermodynamic energy criterion of water splitting [25,26]. As shown in Fig. 1c, $Bi_8(CrO_4)O_{11}$ presents an evidently high surface photovoltage (SPV), and the response range could be extended to about 678 nm, demonstrating its wide-spectrum driven photocatalytic activity. Besides, it exhibits a positive surface photovoltage signal, meaning that the photogenerated holes are the main carriers and transfer to the surface to oxidize reactants. Therefore, the above results indicate that the $Bi_8(CrO_4)O_{11}$ nanorod is a very promising wide-spectrum driven and stable photocatalyst.

Considering that the photocatalytic redox ability mainly depends on the energy band potential, the redox potentials of the $Bi_8(CrO_4)O_{11}$ nanorod photocatalyst were calculated according to the DRS and Mott–Schottky plots (Fig. S5a) [27,28]. As shown in Fig. 1d, the CB of $Bi_8(CrO_4)O_{11}$ is located at 0.12 eV vs. NHE (pH = 0), a little deeper than the reduction potential of $H^+/H_2$. Also, its VB of 1.95 eV is more positive than the oxidation potential of $OH^-/O_2$, which indicates that the photogenerated holes of $Bi_8(CrO_4)O_{11}$ nanorod photocatalyst possess extremely strong oxidation capability, and can split water to release $O_2$, and even completely mineralize organic pollutants under visible light.

We first evaluate the photocatalytic water oxidation performance over $Bi_8(CrO_4)O_{11}$ nanorods. Figure 2a shows a comparison of the photocatalytic $O_2$ evolution rate over different samples. It can be seen that $Bi_8(CrO_4)O_{11}$ exhibited far superior photocatalytic water oxidation performance, and its average $O_2$ evolution rate reached 14.94 $\mu$mol $h^{-1}$, about 11.5 and 4.0 times higher than that of $Bi_2WO_6$ nanosheets [29] and commercial $WO_3$ nanoparticles. Besides, $Bi_8(CrO_4)O_{11}$ consequently achieved a considerable apparent quantum efficiency (AQE) 2.87% at 420 nm, even 0.65% at 650 nm (Fig. 2b), higher than many reported wide-spectrum driven photocatalysts (Table S2). In addition, the trend of

AQE values for water oxidation over $Bi_8(CrO_4)O_{11}$ is also consistent with its UV–vis DRS, further confirming that the photocatalytic water oxidation reaction is driven by its absorbed incident photons. Furthermore, after loading $Co(OH)_2$ as co-catalyst, its photocatalytic water oxidation performance was improved by 2.1 times (Fig. S6). Just as importantly, no notable deactivation emerged over $Bi_8(CrO_4)O_{11}$ during a continuous photocatalytic water oxidation reaction for 72 h (Fig. S7a). By comparing its XRD patterns and XPS results before and after reaction (Figs S7b and S8), it could be found that the crystal structure and composition of $Bi_8(CrO_4)O_{11}$ after reaction show no marked change, further indicating its robust resistance to water and light corrosion.

Most noticeably, the excellent activity of $Bi_8(CrO_4)O_{11}$ is also manifested in photocatalytic degradation of phenol. As shown in Fig. 2c, $Bi_8(CrO_4)O_{11}$ showed a superior photocatalytic degradation performance for phenol under visible light, and its degradation reaction constant could reach $0.119$ min$^{-1}$, about 22.5 and 8.8 times higher than CdS nanowires [30] and N,N′-di(propanoic acid)-perylene-3,4,9,10-tetracarboxylic diimide (PDI) supramolecular [31,32] photocatalysts, respectively. Even its degradation activity is not inferior to P25 $TiO_2$ under simulated sunlight, being about 2.9 times higher than the latter. Remarkably, $Bi_8(CrO_4)O_{11}$ also presented extremely strong mineralization ability, which almost enables simultaneous degradation and complete mineralization for phenol. The total organic carbon (TOC) removal rates of phenol over $Bi_8(CrO_4)O_{11}$ under visible light and simulated sunlight are 94.8% (degradation rate: 95.5%) and 97.3% (degradation rate: 98.1%) in 0.5 h, respectively, while that of CdS, PDI and P25 are significantly lower than their corresponding degradation rates. In particular, even under 650 nm red light irradiation, $Bi_8(CrO_4)O_{11}$ is still able to simultaneously degrade and completely mineralize phenol (Fig. 2d), and few wide-spectrum driven photocatalysts can achieve that [33]. Besides, $Bi_8(CrO_4)O_{11}$ also exhibited highly efficient photocatalytic formaldehyde degradation activity under visible light in a continuous-flow system, and the removal rate could be maintained at about 95% (Fig. S10c). No notable deactivation emerges during continuous measurement for 76 h.

It is well known that photocatalytic activity is closely related to the separation efficiency of photogenerated electron–hole pairs [34–36]. Previous studies have demonstrated that the IEF induced by the crystal dipole is considered to effectively boost the separation of photogenerated electron–hole pairs and enhance the photocatalytic performance exponentially, such as in $Bi_2MoO_6$, $BiPO_4$, and BiOCl [37–39]. Therefore, to reveal the high activity mechanism of $Bi_8(CrO_4)O_{11}$, the crystal dipoles of $Bi_8(CrO_4)O_{11}$ and tetragonal $Bi_{14}CrO_{24}$ nanosheets (Figs S1 and S2) and their influence on the charge carrier separation and photocatalytic activity were studied. Through the Debye equation, the dipole moments of $Bi_8(CrO_4)O_{11}$ and $Bi_{14}CrO_{24}$ were calculated to be 22.32 and 2.52 Debye (D), respectively. As shown in Fig. 3a, due to the existence of the great dipole of $Bi_8(CrO_4)O_{11}$, the distortion of $[BiO_x]$ and $[CrO_y]$ polyhedrons induced an apparently uneven distribution of the electronic cloud between Bi–O and Cr–O, thus resulting in a giant IEF. Then, Kelvin probe force microscopy techniques were employed to reveal the IEF distribution in $Bi_8(CrO_4)O_{11}$ and $Bi_{14}CrO_{24}$. As shown in Fig. 3b, $Bi_8(CrO_4)O_{11}$ shows an obvious difference in the contact potential difference (CPD) between the edge and the bulk, about 202 mV (Fig. 3c), but the CPD difference over $Bi_{14}CrO_{24}$ is virtually invisible, only about 39 mV. According to the literature, the relatively large CPD difference between the two regions reflects that a relatively strong IEF is formed in the crystal [40–42], consequently demonstrating the existence of a greater IEF in $Bi_8(CrO_4)O_{11}$.

Furthermore, the intensity of their IEF was measured via the model developed by Kanata-Kito *et al.* (details are given in the supplementary data online) [43,44]. It can be found that the IEF of $Bi_8(CrO_4)O_{11}$ is 8.4 times as high as that of $Bi_{14}CrO_{24}$ (Fig. S13), well consistent with the above results. Benefiting from its greater IEF, $Bi_8(CrO_4)O_{11}$ presented an evidently stronger surface photovoltage response and photocurrent density (Fig. S16), about 22.7 and 4.0 times higher than $Bi_{14}CrO_{24}$, respectively, revealing that a faster charge carrier transfer kinetics emerges in $Bi_8(CrO_4)O_{11}$. As expected, $Bi_8(CrO_4)O_{11}$ exhibited 17.2 and 153.0 times higher photocatalytic water oxidation and degradation performance than $Bi_{14}CrO_{24}$, respectively. Then, after summarizing the above results into Fig. 3d, it can be found that the IEF, charge separation efficiency and photocatalytic activity of bismuth chromate are positively correlated with their dipole moments; thus $Bi_8(CrO_4)O_{11}$ with a greater dipole showed a significantly higher IEF, charge separation efficiency and photocatalytic performance. Therefore, as illustrated in Scheme 1, the large crystal dipole of $Bi_8(CrO_4)O_{11}$ induces a giant IEF, which accelerates the rapid separation of photogenerated electron–hole pairs and exponentially enhances its photocatalytic performance. Most importantly, based on the above mechanism, many more efficient photocatalysts can be designed successfully by regulating the crystal dipole.
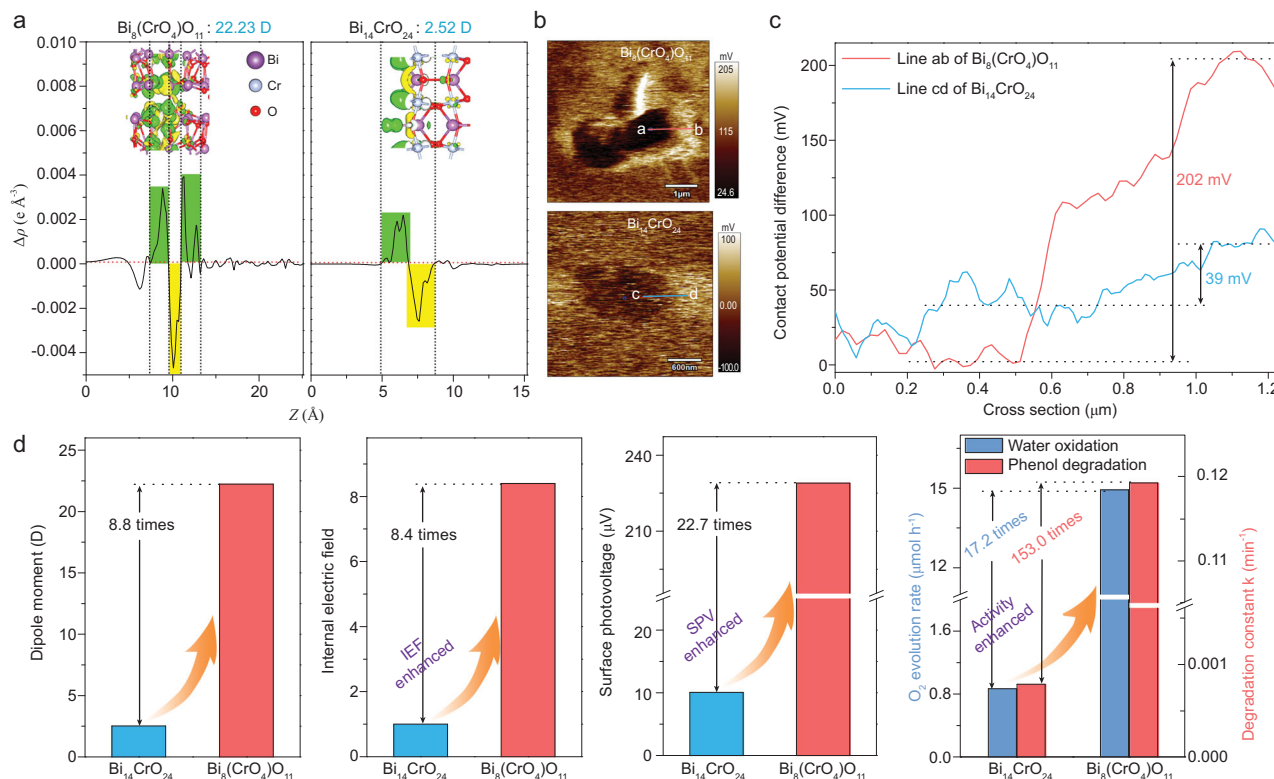
**Figure 3.** (a) A side view of the charge density difference and planar-averaged electron density difference $\Delta\rho(z)$ (the yellow and green areas indicate electron depletion and accumulation, respectively), (b) the surface potential image in the dark state, (c) the cross section of the surface potential distribution along the blue line ab and cd in (b) and (d) the correlation between dipole moments, internal electric field intensity, surface photovoltage and photocatalytic activity of $Bi_8(CrO_4)O_{11}$ and $Bi_{14}CrO_{24}$.
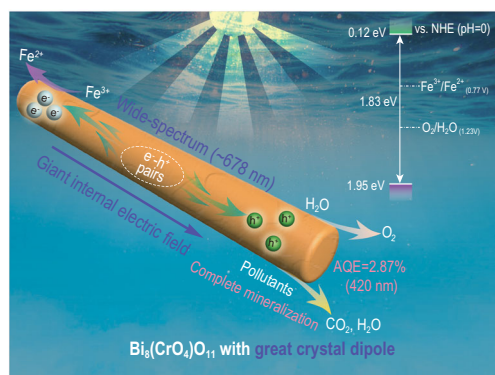


**Scheme 1.** Schematic mechanism of the photocatalytic reaction over $Bi_8(CrO_4)O_{11}$.

## CONCLUSION

In conclusion, a wide-spectrum ($\sim$678 nm) responsive $Bi_8(CrO_4)O_{11}$ nanorod photocatalyst was constructed via the hybridization of Cr 3d with O 2p orbitals. Attributed to the giant IEF induced by its large dipole moment, $Bi_8(CrO_4)O_{11}$ realizes evidently rapid separation of photogenerated electron–hole pairs, thus showing highly efficient photocatalytic water oxidation performance with a notable apparent quantum yield of 2.87% (420 nm), superior to many reported wide-spectrum driven photocatalysts. Most remarkably, its strong oxidation ability also enables simultaneous degradation and complete mineralization for phenol, and its excellent performance is about 23.0 and 2.9 times higher than CdS and P25-TiO$_2$, respectively. Briefly, the discovery of wide-spectrum bismuth chromate and the mechanism of exponentially enhanced photocatalytic performance by increasing the crystal dipole throw light on designing efficient wide-spectrum photocatalysts.

## METHODS

### Synthesis of samples

NaBiO$_3$ and other chemicals were purchased from Aladdin and Sigma-Aldrich, respectively, and used without further purification. For $Bi_8(CrO_4)O_{11}$ nanorods, 0.56 g NaBiO$_3$ was ultrasonically dispersed in 80 mL deionized water, followed by addition of 7.35 mL 25 mmol L$^{-1}$ Cr(NO)$_3$ aqueous solution under vigorous stirring. Then the resulting solution was transferred into a 100 mL

Teflon-lined stainless autoclave and maintained at 180°C for 6 h. The brown-red $Bi_8(CrO_4)O_{11}$ was collected by centrifuge separation, rinsed thoroughly with ethanol and deionized water several times, and dried at 70°C overnight. For $Bi_{14}CrO_{24}$ nanosheets, 1 mmol $Bi(NO_3)_3$ and 0.084 mmol $Cr(NO_3)_3$ were ultrasonically dissolved in a certain concentration of mannitol aqueous solution (25 mL), followed by addition of 5 ml saturated $Na_2CO_3$ solution under vigorous stirring. Then the resulting solution was transferred into a 50 mL Teflon-lined stainless autoclave and maintained at 150°C for 12 h. The precursor was collected by centrifuge separation, rinsed thoroughly with ethanol and deionized water several times, and dried at 70°C overnight. The precursor was then calcined in a crucible at a certain temperature for 10 min under air atmosphere to yield orange-red $Bi_{14}CrO_{24}$ nanosheets.

For comparison, $BiWO_6$ nanoplates were synthesized as in [29], and $WO_3$ nanoparticles were purchased from Aladdin.

## Characterization

XRD patterns of the samples were obtained on a Rigaku D/max-2400 X-ray diffractometer using Cu K$\alpha$1 ($\lambda$ = 0.154 18 nm) at 40 kV and 200 mA, with a scan step of 0.02°. The morphologies of the samples were measured by transmission electron microscopy (TEM) on a Hitachi HT 7700 at an accelerating voltage of 100 kV and high-resolution transmission electron microscopy (HRTEM) on a JEOL JEM-2100F operated at an accelerating voltage of 200 kV. Field emission scanning electron microscopy (FESEM) on a Hitachi SU-8010 was used to further investigate the morphology. XPS measurements were performed using an ESCALAB 250Xi instrument (Thermo Scientific) with Al K$\alpha$ radiation. DRS were obtained on a Cary 5000 (Varian) with $BaSO_4$ as a reference. The surface potential images of the samples were measured by Kelvin probe force microscopy (KPFM) in ambient atmosphere on a Cypher VRS (Oxford Instruments) and a Pt/Ir-coated Si tip was used as a Kelvin tip. The surface photovoltage measurements were conducted with a home-built instrument as previously reported [45]. Photoelectrochemical measurements were performed on a CHI660E electrochemical workstation, using a standard three-electrode cell with a working electrode, a Pt-wire counter electrode and a saturated calomel reference electrode. $Na_2SO_4$ (0.1 mol L$^{-1}$) was used the electrolyte solution. The working electrode was prepared by dip-

coating photocatalyst slurry on ITO glass electrode (2 × 4 cm$^2$).

## Photocatalytic performance evaluation

The photocatalytic water oxidation reaction under visible-light irradiation was performed in a Pyrex top-irradiation reaction vessel with a stationary temperature at 5°C, which was connected to a glass closed gas system (Labsolar-6A, PerfectLight). 100 mg photocatalyst was suspended individually in 100 mL aqueous solution (pH = 2.5) containing 10 mmol L$^{-1}$ $Fe(NO_3)_3$ as a sacrificial reagent. The suspension was then thoroughly degassed and irradiated using a 300 W Xe lamp with a cut-off filter ($\lambda \geq$ 420 nm, light intensity 250–260 mW cm$^{-2}$). The evolved gases were analyzed at given time intervals by an online gas chromatograph (GC-2002 N/TFF, TCD detector, Ar carrier, 5 Å molecular sieve column).

The AQE for water oxidation was measured using a 300 W Xe lamp (FX300, PerfectLight) with different band-pass filters of 420, 450, 500, 550, 600, and 650 nm (FWHM = 15 nm). The irradiation area was controlled as 1.2 × 1.2 cm$^2$. The average intensity was determined by an optical power meter (S310C connected to a PM100D console, Thorlabs). The AQE was calculated as follows:

$$AQE = \frac{4 \times \text{the number of evolved } O_2 \text{ molecules}}{\text{the number of incident photons}} \times 100\%.$$

The photodegradation reactions were carried in quartz tube reactors with a 50 mL 10 ppm phenol pollutant solution and 25 mg photocatalyst powders. The reaction solution was kept at 35°C by a recirculating cooling water system. The visible-light source was obtained from a 300 W Xe lamp with a cut-off filter ($\lambda \geq$ 420 nm). Before light irradiation, the suspension solutions were first ultrasonically dispersed for 5 min and then magnetically stirred for 1 h in the dark to reach adsorption–desorption equilibrium. At certain time intervals, a suspension (2 mL) was extracted and centrifuged to remove the photocatalysts. The concentration of phenol pollutants was determined by a high-performance liquid chromatography (HPLC) system (Shimadzu LC-20AT) with a C18 reversed-phase column, and the total organic carbon (TOC) in the aqueous solution was analyzed using a TOC analyzer (Multi N/C 2100, Analytik Jena AG).

## REFERENCES

1. Tong H, Ouyang S and Bi Y *et al.* Nano-photocatalytic materials: possibilities and challenges. *Adv Mater* 2012; **24**: 229–51.
2. Hoffmann MR, Martin ST and Choi W *et al.* Environmental applications of semiconductor photocatalysis. *Chem Rev* 1995; **95**: 69–96.
3. Hisatomi T and Domen K. Reaction systems for solar hydrogen production via water splitting with particulate semiconductor photocatalysts. *Nat Catal* 2019; **2**: 387–99.
4. Ma Y, Wang X and Jia Y *et al.* Titanium dioxide-based nanomaterials for photocatalytic fuel generations. *Chem Rev* 2014; **114**: 9987–10043.
5. Garcia-Esparza AT, Shinagawa T and Ould-Chikh S *et al.* An oxygen-insensitive hydrogen evolution catalyst coated by a molybdenum-based layer for overall water splitting. *Angew Chem Int Ed* 2017; **56**: 5780–4.
6. Kato H, Asakura K and Kudo A. Highly efficient water splitting into $H_2$ and $O_2$ over lanthanum-doped $NaTaO_3$ photocatalysts with high crystallinity and surface nanostructure. *J Am Chem Soc* 2003; **125**: 3082–9.
7. Zhang P, Ochi T and Fujitsuka M *et al.* Topotactic epitaxy of $SrTiO_3$ mesocrystal superstructures with anisotropic construction for efficient overall water splitting. *Angew Chem Int Ed* 2017; **56**: 5299–303.
8. Maeda K, Teramura K and Lu D *et al.* Noble-metal/$Cr_2O_3$ core/shell nanoparticles as a cocatalyst for photocatalytic overall water splitting. *Angew Chem Int Ed* 2006; **45**: 7806–9.
9. Shi R, Ye HF and Liang F *et al.* Interstitial P-doped CdS with long-lived photogenerated electrons for photocatalytic water splitting without sacrificial agents. *Adv Mater* 2018; **30**: 1705941.
10. Chowdhury FA, Trudeau ML and Guo H *et al.* A photochemical diode artificial photosynthesis system for unassisted high efficiency overall pure water splitting. *Nat Commun* 2018; **9**: 1707.
11. Jiao X, Chen Z and Li X *et al.* Defect-mediated electron-hole separation in one-unit-cell $ZnIn_2S_4$ layers for boosted solar-driven $CO_2$ reduction. *J Am Chem Soc* 2017; **139**: 7586–94.
12. Cui J, Liu T and Qi Y *et al.* A wide visible light driven complex perovskite Ba $(Mg_{1/3}Ta_{2/3})O_{3-x}N_y$ photocatalyst for water oxidation and reduction. *J Mater Chem A* 2017; **5**: 18870–7.
13. Abeysinghe D and Skrabalak SE. Toward shape-controlled metal oxynitride and nitride particles for solar energy applications. *ACS Energy Lett* 2018; **3**: 1331–44.
14. Hisatomi T, Katayama C and Moriya Y *et al.* Photocatalytic oxygen evolution using $BaNbO_2N$ modified with cobalt oxide under photoexcitation up to 740 nm. *Energ Environ Sci* 2013; **6**: 3595–9.
15. Maeda K, Lu D and Domen K. Oxidation of water under visible-light irradiation over modified $BaTaO_2N$ photocatalysts promoted by tungsten species. *Angew Chem Int Ed* 2013; **52**: 6488–91.
16. Wang L, Xu K and Cui W *et al.* Monolayer epitaxial heterostructures for selective visible-light-driven photocatalytic NO oxidation. *Adv Funct Mater* 2019; **29**: 1808084.
17. Li P, Chen X and He H *et al.* Polyhedral 30-faceted $BiVO_4$ microcrystals predominantly enclosed by high-index planes promoting photocatalytic water-splitting activity. *Adv Mater* 2018; **30**: 1703119.
18. Cao S, Shen B and Tong T *et al.* 2D/2D heterojunction of ultrathin MXene/$Bi_2WO_6$ nanosheets for improved photocatalytic $CO_2$ reduction. *Adv Funct Mater* 2018; **28**: 1800136.
19. Zhou Y, Zhang Y and Lin M *et al.* Monolayered $Bi_2WO_6$ nanosheets mimicking heterojunction interface with open surfaces for photocatalysis. *Nat Commun* 2015; **6**: 8340.
20. Li D, Liu Y and Shi W *et al.* Crystallographic-orientation-dependent charge separation of $BiVO_4$ for solar water oxidation. *ACS Energy Lett* 2019; **4**: 825–31.
21. Kong HJ, Won DH and Kim J *et al.* Sulfur-doped g-$C_3N_4$/$BiVO_4$ composite photocatalyst for water oxidation under visible light. *Chem Mater* 2016; **28**: 1318–24.
22. Wang Q, Hisatomi T and Suzuki Y *et al.* Particulate photocatalyst sheets based on carbon conductor layer for efficient Z-scheme pure-water splitting at ambient pressure. *J Am Chem Soc* 2017; **139**: 1675–83.
23. Zhao Y, Zhang S and Li B *et al.* A family of visible-light responsive photocatalysts obtained by dispersing $CrO_6$ octahedra into a hydrotalcite matrix. *Chem Eur J* 2011; **17**: 13175–81.
24. Silva CG, Bouizi Y and Fornés V *et al.* Layered double hydroxides as highly efficient photocatalysts for visible light oxygen generation from water. *J Am Chem Soc* 2009; **131**: 13833–9.
25. Chen S, Takata T and Domen K. Particulate photocatalysts for overall water splitting. *Nat Rev Mater* 2017; **2**: 17050.
26. Kong D, Zheng Y and Kobielusz M *et al.* Recent advances in visible light-driven water oxidation and reduction in suspension systems. *Mater Today* 2018; **21**: 897–924.
27. Gelderman K, Lee L and Donne S. Flat-band potential of a semiconductor: using the Mott–Schottky equation. *J Chem Educ* 2007; **84**: 685–8.
28. Tao X, Zhao Y and Mu L *et al.* Bismuth tantalum oxyhalogen: a promising candidate photocatalyst for solar water splitting. *Adv Energy Mater* 2018; **8**: 1701392.
29. Zhang C and Zhu Y. Synthesis of square $Bi_2WO_6$ nanoplates as high-activity visible-light-driven photocatalysts. *Chem Mater* 2005; **17**: 3537–45.
30. Jiang W, Liu Y and Zong R *et al.* Photocatalytic hydrogen generation on bifunctional ternary heterostructured $In_2S_3$/$MoS_2$/CdS composites with high activity and stability under visible light irradiation. *J Mater Chem A* 2015; **3**: 18406–12.

31. Liu D, Wang J and Bai X *et al.* Self-assembled PDINH supramolecular system for photocatalysis under visible light. *Adv Mater* 2016; **28**: 7284–90.

32. Wang J, Shi W and Liu D *et al.* Supramolecular organic nanofibers with highly efficient and stable visible light photooxidation performance. *Appl Catal B Environ* 2017; **202**: 289–97.

33. Yang MQ, Gao M and Hong M *et al.* Visible-to-NIR photon harvesting:progressive engineering of catalysts for solar-powered environmental purification and fuel production. *Adv Mater* 2018; **30**: 1802894.

34. Chen X, Shi R and Chen Q *et al.* Three-dimensional porous g-C$_3$N$_4$ for highly efficient photocatalytic overall water splitting. *Nano Energy* 2019; **59**: 644–50.

35. Che W, Cheng W and Yao T *et al.* Fast photoelectron transfer in (Cring)-C$_3$N$_4$ plane heterostructural nanosheets for overall water splitting. *J Am Chem Soc* 2017; **139**: 3021–6.

36. Chen R, Pang S and An H *et al.* Charge separation via asymmetric illumination in photocatalytic Cu$_2$O particles. *Nat Energy* 2018; **3**: 655–63.

37. Morris MR, Pendlebury SR and Hong J *et al.* Effect of internal electric fields on charge carrier dynamics in a ferroelectric material for solar energy conversion. *Adv Mater* 2016; **28**: 7123–8.

38. Li J, Cai L and Shang J *et al.* Giant enhancement of internal electric field boosting bulk charge separation for photocatalysis. *Adv Mater* 2016; **28**: 4059–64.

39. Jiang J, Zhao K and Xiao X *et al.* Synthesis and facet-dependent photoreactivity of BiOCl single-crystalline nanosheets. *J Am Chem Soc* 2012; **134**: 4473–6.

40. Zhu J, Pang S and Dittrich T *et al.* Visualizing the nano cocatalyst aligned electric fields on single photocatalyst particles. *Nano Lett* 2017; **17**: 6735–41.

41. Zhu J, Fan F and Chen R *et al.* Direct imaging of highly anisotropic photogenerated charge separations on different facets of a single BiVO$_4$ photocatalyst. *Angew Chem Int Ed* 2015; **54**: 9111–4.

42. Chen R, Fan F and Dittrich T *et al.* Imaging photogenerated charge carriers on surfaces and interfaces of photocatalysts with surface photovoltage microscopy. *Chem Soc Rev* 2018; **47**: 8238–62.

43. Kanata-Kito T, Matsunaga M and Takakura H *et al.* Photoreflectance characterization of built-in potential in MBE-produced as-grown GaAs surface. *Proc SPIE* 1990; **1286**: 56–66.

44. Lefebvre P, Allègre J and Gil B *et al.* Time-resolved photoluminescence as a probe of internal electric fields in GaN-(GaAl)N quantum wells. *Phys Rev B* 1999; **59**: 15363–7.

45. Zhang Z, Zhu Y and Chen X *et al.* A full-spectrum metal-free porphyrin supramolecular photocatalyst for dual functions of highly efficient hydrogen and oxygen evolution. *Adv Mater* 2019; **31**: 1806626.